Originally published as:

Receiver functions at the stations of the German Regional Seismic Network (GRSN)

R. Kind,[1] G. L. Kosarev[2] and N. V. Petersen[2]

[1]GeoForschungsZentrum, Telegrafenberg A6, 14473 Potsdam, Germany
[2]Institute of the Physics of the Earth, Russian Academy of Sciences, B. Gruzinskaya 10, 123810 Moscow, Russia

SUMMARY

Several years of broad-band teleseismic data from the GRSN stations have been analysed for crustal structure using P-to-S converted waves at the crustal discontinuities. An inversion technique was developed which applies the Thomson–Haskell formalism for plane waves without slowness integration. The main phases observed are Moho conversions, their multiples in the crust, and conversions at the base of the sediments. The crustal thickness derived from these data is in good agreement with results from other studies. For the Gräfenberg stations, we have made a more detailed comparison of our model with a previously published model obtained from refraction seismic experiments. The refraction seismic model contains boundaries with strong velocity contrasts and a significant low-velocity zone, resulting in teleseismic waveforms that are too complicated as compared to the observed simple waveforms. The comparison suggests that a significant low-velocity zone is not required and that internal crustal boundaries are rather smooth.

Key words: converted waves, crustal structure, receiver function.

INTRODUCTION

The usual methods to explore the crustal and lithospheric structures by seismic methods are steep-angle (reflection) and wide-angle (refraction) methods. The reflection and refraction methods also potentially have the highest resolution because of the relatively high frequency of the seismic waves used. Long-period surface waves have much lower resolution, but penetrate deeper into the mantle. The frequency band between the controlled source methods (several Hertz) and the surface-wave methods (many seconds) is covered by teleseismic body-wave methods (periods of one or a few seconds). Teleseismic body waves have been used intensively for a long time to investigate the crustal structure (crustal transfer method: e.g. Phinney 1964). Improvements of the method have been applied by Burdick & Langston (1977) and Vinnik & Kosarev (1981). Owens, Zandt & Taylor (1984) further improved the method for application of the newly available broad-band data. It is now commonly referred to as the receiver function method. A nice numerical discussion is given by Cassidy (1992). Parallel to these developments was a method developed for detecting weak converted waves (Vinnik 1977). This method was mainly applied to upper mantle studies (e.g. Kind & Vinnik 1988; Stammler et al. 1992).

Kosarev, Makeyera & Vinnik (1987) added an inversion technique to the observational part of Vinnik's method. An example of an application is given by Kosarev et al. (1993).

This rather long history of the receiver function method has established its usefulness. The main results obtained by the receiver function method are shear-wave models of the crust, and information about crustal discontinuities (Moho, bottom of sediments, Conrad) and steepness of gradients. Usually, multiple reflections are also observed in the crust. Their waveforms must also be explained by inverted crustal models. Models obtained from controlled source experiments must also be able to explain the observed long-period receiver function. Therefore, the receiver function method can also serve as a check for crustal models obtained with higher resolution methods.

ANALYSIS METHOD

The theoretical background of the technique used to analyse the waveforms is described earlier (Vinnik 1977; Kosarev et al. 1987; Petersen & Vinnik 1991; Kosarev et al. 1993). The method uses P-to-S converted waves at discontinuities underneath a seismic station. It consists of two steps. The data are first processed in order to produce stable observations. The second step consists of the inversion of

the observations using complete theoretical plane-wave seismograms.

The essential points in processing the observed data follow.

(1) Rotation of the original Z, NS and EW components of the P-wave group into the ray coordinate system L, Q and T.

L contains mainly P-energy, Q mainly SV-energy, and T mainly SH-energy. The energy on the T-component at the time of the P-wave group gives an indication about the presence of anisotropy or lateral heterogeneity. The theoretical backazimuth is used to determine the radial component, and the angle of incidence is determined from the radial–vertical covariance matrix of the P-signal of the original data (Vinnik 1977; Kanasewich 1981). The Q-component contains the information in which we are mainly interested, the P-to-SV converted energy. This energy depends mainly on the S-velocity distribution underneath the station.

(2) Deconvolution of the Q- and T-components with the P-signal on the L-component.

In this study, deconvolution was used instead of the cross-correlation used in the earlier version of the method. Deconvolution has turned out to be more efficient (Stammler et al. 1992; Petersen et al. 1993) in attaining a higher resolution of the signal. Deconvolution is also used as a source-equalization procedure because it excludes effects of the rupture process and of the ray-path below the converting interfaces. Differences in the source durations and magnitudes are equalized, permitting the summation of many different events. Amplitude ratios are preserved by this procedure. The deconvolution method by Berkhout (1977) was chosen, which generates the inverse filter in the time domain by minimizing the least-squares difference between the actual output and the desired delta-like spike function of normalized amplitude. The P waveform on the L-component is used to generate the deconvolution filter. After deconvolution, all components are normalized to the maximum of L.

(3) Summation of many events from a large distance and azimuth range.

The summation of rotated and deconvolved records from earthquakes with epicentres in a broad azimuth and distance range is used to improve the signal-to-noise ratio and therefore the stability and reliability of the observations. This kind of summation results in a flat and averaged crustal model. If the azimuthal coverage is sufficiently dense, studies of effects depending on the azimuth are possible, indicating anisotropy or lateral heterogeneity. The summation of events from a broad distance range permits the determination of the slowness (or apparent slowness in the case of dipping interfaces) of the incoming P and converted phases. Summation is an important tool in studies of conversions from discontinuities in the upper mantle (Vinnik 1977), because the slowness of these phases is different enough for it to be resolved from the P slowness. For conversions from the Moho this is, however, not the case. Therefore summation over events from many distances is used in crustal studies only to improve the signal-to-noise ratio, and to increase the reliability of the observations. The averaged epicentral distance of all events was used as the epicentral distance of the summation seismogram.

INVERSION METHOD

We consider the theoretical L- and Q-components of the teleseismic P wave computed on the Earth's surface, and assume that the Earth's crust can be modelled by a stack of plane homogeneous layers over a homogeneous half-space. The P wave is considered to be a plane wave with apparent velocity c, determined from the epicentral distance and the depth of the event to be modelled. The expression for the synthetic SV component for a given layered structure can then be calculated by the formula

$$Q_{syn}(t, v(d), c) = \frac{1}{2\pi} \int_{-\infty}^{\infty} \frac{H_Q(\omega, v(d), c)}{H_L(\omega, v(d), c)} L(\omega) \exp(i\omega t) \, d\omega,$$

where $v(d)$ is the starting velocity-depth function, which also can be presented as a vector of the variable model parameters, c is the apparent velocity, $H_Q(\omega, v(d), c)$ and $H_L(\omega, v(d), c)$ are the SV and P components of the theoretical frequency response of the layered structure, and $L(\omega)$ is the spectrum of the primary P wave.

The observed Q-component Q_{obs} is the sum of all Q-components used. The apparent velocity needed for the computation of the theoretical seismograms (Haskell 1962) is obtained from the averaged epicentral distance. For rotation of the theoretical Z- and R-components into the L and Q system, the same procedure as for the observed seismograms was used; i.e., the rotation angle is obtained from the covariance matrix. The model $v(d)$ can be tested by comparing $Q_{syn}(v(d), t)$ with $Q_{obs}(t)$. The search for the best-fitting model can be made in a number of ways. The main difficulties occurring in the inversion procedure are typical for many geophysical inversion problems: non-uniqueness, instability, and proper choice of parameters. Our inversion procedure is based on the general method of solving ill-posed inverse problems (Tikhonov & Arsenin 1979; Glasko 1984). The optimum parameters of the model can be found by iterative minimization of the smoothing functional:

$$F(v(d), c) = \|Q_{obs}(t) - Q_{syn}(v(d), t, c)\|$$
$$+ \alpha q(d) \| v(d) - v_0(d) \|,$$

where $v_0(d)$ is the starting velocity model, $q(d)$ is the weight function and α is the damping parameter. (The vertical double bars designate the mean-square deviation.) The parameter α changes during the inversion procedure as $\alpha_{p+1} = \alpha_p \Delta \alpha$, where α_p is the value of α in the preceding iteration, and $\Delta \alpha \leq 1$. Normally, we used $q(d) = 1$, $\alpha_0 = 100$ and $\Delta \alpha = 0.3$. If this procedure was not successful, that is the minimization failed or the values of optimal parameters were too unreasonable, we changed the values $q(d)$, α_0 or $\Delta \alpha$, the parameters of the starting model, or used the usual trial and error method. The mean-square error of the fit is given in the same units as the data, that is in per cent of the P-signal.

COMPARISON OF PLANE-WAVE AND REFLECTIVITY THEORETICAL SEISMOGRAMS

The theoretical seismograms used in the inversion method have been computed with the Thomson–Haskell method for
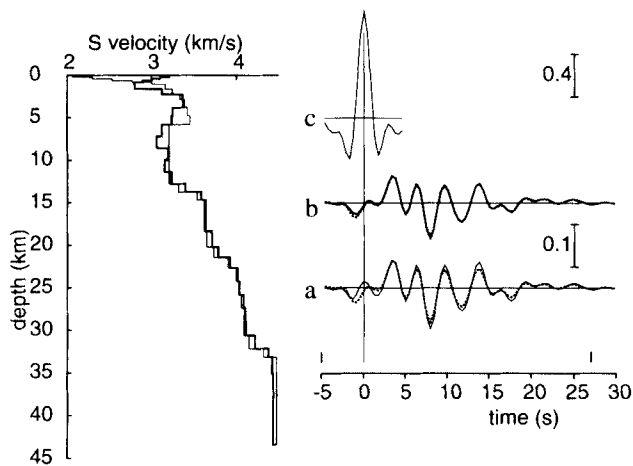
Figure 1. Comparison of plane-wave and reflectivity seismograms (*Q*-components). The dashed lines in a and b are the distance-averaged reflectivity seismograms. The continuous line in a is the corresponding plane-wave seismogram. The continuous line in b is the plane-wave seismogram resulting from inverting the reflectivity seismogram. The inversion yields the *S*-velocity model shown by the thick solid line. The starting *S*-velocity–depth model is indicated by the thin solid line, which is the refraction seismic model of Aichele (1976). Trace c is the deconvolved *P*-signal on the *L*-component. Normalized amplitudes are indicated by the vertical bars. The vertical lines above the time-scale mark the inversion interval.

just one slowness. No slowness integration was used (the reflectivity method, in contrast, does use such an integration). Therefore this method is a plane-wave method. For verification, we computed a suite of theoretical seismograms with the reflectivity method between 40° and 90° epicentral distance. The reflectivity seismograms are treated like observed seismograms (they are rotated, deconvolved and summed). The summed *Q*-components are the dashed lines in Fig. 1, traces a and b. The Thomson–Haskell seismogram at the averaged distance of 65° is also shown as a continuous line a in Fig. 1. The two traces in a show some differences. We cannot expect complete agreement, since the two methods have several differences. A comparison of the two traces a in Fig. 1 shows how much similarity between observed and synthetic traces the method permits under ideal circumstances. Next, the reflectivity seismograms have been inverted using the plane-wave method (traces b) in Fig. 1. These two lines now agree nearly perfectly; however, the model used for the reflectivity method (thin line in the velocity model in Fig. 1) and the inverted model (thick line) are somewhat different. These differences are due to a systematic error in the method. It seems to be tolerably small. Trace c in Fig. 1 shows the deconvolved *P* wave of the reflectivity seismograms. It was used as an input signal for the Thomson–Haskell seismogram. The model used for the comparison in Fig. 1 is obtained from Aichele (1976), except that the mantle velocity was chosen to be somewhat lower (thin line).

DATA

The data used in this study are three-component teleseismic *P* waveforms in the 30 s time interval starting from the *P*-wave onset. Extending the intervals up to 100 s did not

change the results. The waveforms were recorded by the high-quality broad-band digital regional seismic network of the Federal Republic of Germany, GRSN. At present, we can use the records of 11 seismic stations. Three stations—GRA1, GRB1, GRC1—are part of the Gräfenberg (GRF) array and started their operation in 1977. Eight stations started their operation in 1991 (see Fig. 2). These stations are HAM (Hamburg), BRNL (Berlin), BUG (Bochum), CLZ (Clausthal-Zellerfeld), TNS (Taunus), BFO (Black Forest), FUR (Fürstenfeldbruck) and WET (Wetzell). All GRSN stations are equipped with Streckeisen (STS-2) three-component broad-band seismometers, and the GRF stations have STS-1 instruments.

An important procedure was the selection of events used for further processing. We have chosen low-noise seismograms with simple pulse-like waveforms on the vertical component. Epicentral distances range from 35° to 100°. Table 1 contains the list of events used. The first 53 events are recorded only by the GRF stations.

As a data example, we show the whole set of equalized *Q*-components for FUR (Fig. 3) and BRNL (Fig. 4). From these figures, we see that:

the similarity of the waveforms from different events is clear (especially at FUR, despite a rather high noise level);

the stacked waveforms at FUR and BRNL are different, implying that the receiver structures at these stations are different;

the differences in the records at a station are probably mainly due to azimuthal variations, and they are obviously larger at BRNL than at FUR.

At FUR, the two clear pulses are the conversions at the base of the sediments and the Moho discontinuity. At BRNL, the one broad pronounced pulse at the beginning of the records is a consequence of the thick low-velocity sedimentary layer. We can see no clear conversion from the Moho.

Fig. 5 shows the whole set of the stacked *Q*-components (solid lines) and *T*-components (dashed lines) for all 11 stations. Some conclusions can be drawn from the analysis of Fig. 5:

for all stations, the transverse components have less energy than the *SV*-components;

the amplitude of the transverse component at the Gräfenberg array is smaller than at other GRSN stations. The reason for this difference is the different number of stacked events. For Gräfenberg, the errors in the waveforms and inverted velocity-depth functions are smaller than for the rest of the stations;

the stations with the highest noise level are the GRSN stations with thick, low-velocity sediments: BRNL, HAM, FUR. This can easily be seen from the amplitudes of the *Q*- and *T*-components in the time interval from −10 to 0 s before the *P*-wave onset;

at the stations TNS, CLZ and BUG, the *T*-components have comparable size to the *Q*-components, indicating noticeable horizontal inhomogeneities in the crust under these stations;

different amplitudes of the *Q*-components at different stations imply different amounts of converted energy at the stations and discontinuities.

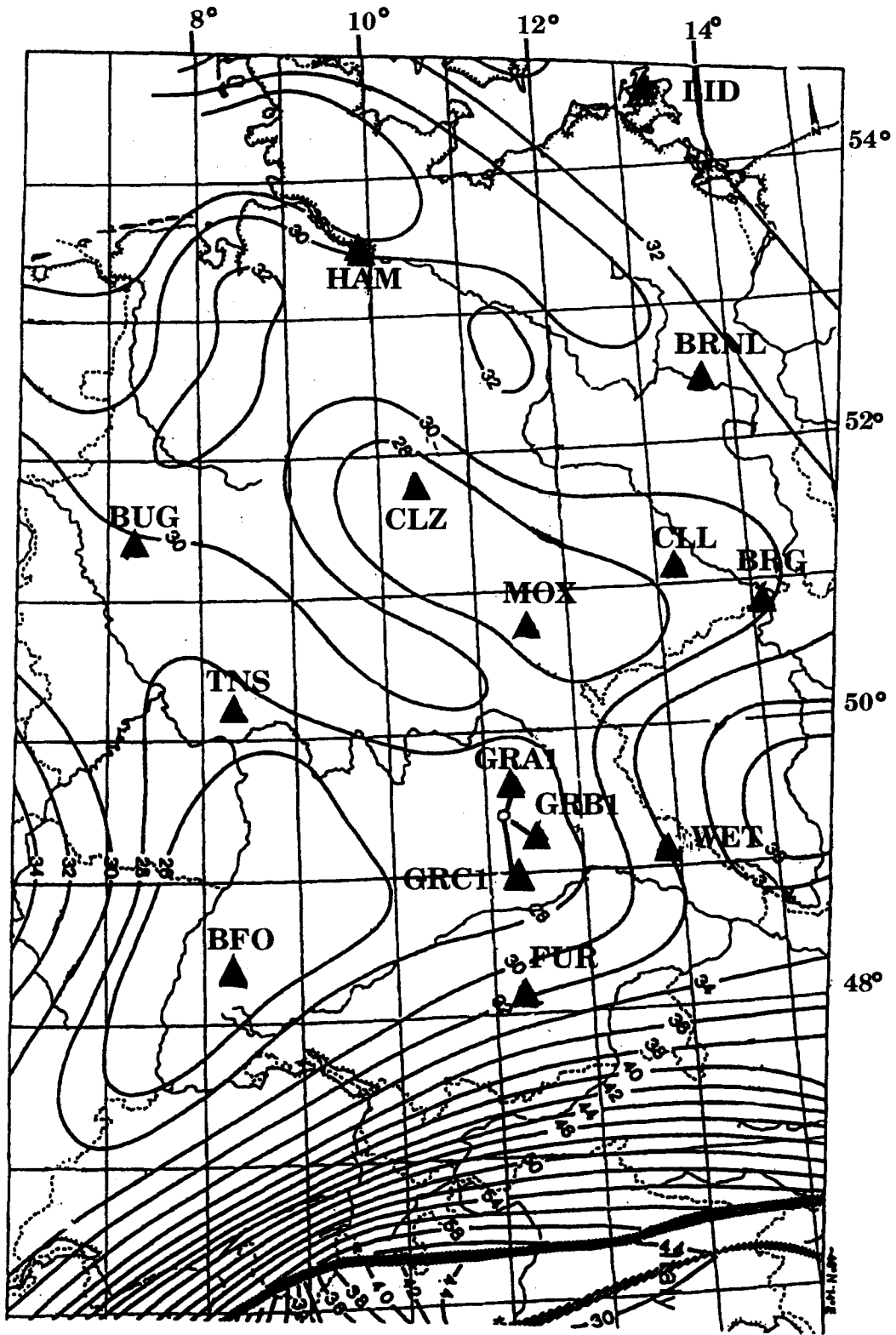At present, the reliable analysis of an azimuthal dependence

Figure 2. The locations of the GRSN stations and isolines of Moho depth in central Europe (Blundell, Freeman & Mueller 1992, based on seismic evidence), contoured in km. The stations LID, MOX, CLL and BRG did not have a sufficient amount of data when this study was conducted.

Table 1. List of events used.

| No.	Date	Origin Time	Latitude (°)	Longitude (°)	Depth (km)	m_b
1	09 Mar 1977	14:27:56.2	47.7N	131.1E	556	5.9
2	04 Sep 1977	15:40:55.0	51.1N	178.4E	20	5.6
3	16 Aug 1979	21:31:24.9	41.9N	130.9E	566	5.8
4	24 Aug 1979	04:26:54.5	9.0N	83.5W	43	5.2
5	24 Aug 1979	16:59:28.9	41.2N	108.1E	18	5.6
6	27 May 1980	14:51:00.3	37.5N	118.8W	22	5.7
7	05 Jul 1980	20:25:25.2	41.9N	77.4E	22	5.4
8	22 Jan 1981	19:34:43.0	38.3N	142.7E	35	6.1
9	04 Sep 1981	11:15:13.9	9.9N	124.0E	651	6.0
10	12 Sep 1981	07:15:53.8	35.7N	73.6E	30	6.2
11	25 Oct 1981	03:22:16.0	18.2N	102.0E	28	6.2
12	01 Jul 1982	07:41:53.7	51.4N	179.9W	51	6.3
13	04 Jul 1982	01:20:08.2	27.9N	137.0E	554	6.2
14	31 Jul 1982	06:29:13.2	51.8N	176.1E	18	6.2
15	24 Jan 1983	23:09:21.7	12.9N	93.6E	81	6.1
16	14 Feb 1983	08:10:04.3	55.0N	159.2W	37	6.0
17	30 Apr 1983	14:03:48.4	41.5N	144.0E	76	6.7
18	01 May 1983	18:10:40.7	46.4N	153.4E	24	6.1
19	02 May 1983	23:42:37.7	36.2N	120.3W	7	6.2
20	02 Jun 1983	20:12:50.9	9.5S	71.2W	600	5.8
21	09 Jun 1983	12:49:02.7	40.3N	139.0E	22	6.3
22	09 Jun 1983	18:46:04.2	51.4N	174.1W	46	6.1
23	10 Jun 1983	02:13:23.2	75.5N	127.8E	10	5.5
24	21 Jun 1983	14:48:07.9	24.1N	122.4E	43	5.8
25	24 Jun 1983	07:18:22.3	21.8N	103.3E	18	6.0
26	24 Jun 1983	09:06:46.3	24.2N	122.4E	48	6.0
27	28 Jun 1983	03:25:16.7	60.2N	141.3W	14	5.9
28	07 Jul 1983	20:35:37.4	7.4S	27.9E	10	5.8
29	22 Dec 1983	04:11:28.4	12.0N	13.6W	3	6.6[J]
30	06 Mar 1984	02:17:21.2	29.4N	138.9E	457	6.2
31	20 Apr 1984	06:31:10.6	50.1N	148.7E	582	6.0
32	23 Apr 1984	21:40:35.6	47.5N	146.7E	414	6.0
33	24 Apr 1984	04:11:29.0	30.9N	138.4E	403	6.1
34	26 Oct 1984	20:22:21.8	39.2N	71.3E	33	6.0
35	01 May 1985	13:27:56.1	9.2S	71.2W	600	6.0
36	06 May 1985	03:04:22.7	30.9N	70.3E	37	5.6
37	14 May 1985	13:24:57.8	10.6S	41.4E	10	6.0
38	14 May 1985	18:11:08.9	10.5S	41.4E	10	6.4
39	16 May 1985	14:20:25.1	29.1S	77.7E	10	5.9
40	06 Jun 1985	02:40:12.9	0.9N	28.4W	10	6.3
41	05 Oct 1985	15:24:00.7	62.1N	124.3W	3	6.5
42	23 Dec 1985	05:16:02.9	62.2N	124.3W	3	6.7
43	26 Apr 1986	07:35:16.0	32.1N	76.3E	33	5.5
44	30 Apr 1986	07:07:15.4	18.6N	102.8W	3	6.4
45	06 Jul 1986	19:24:26.3	34.4N	80.1E	33	5.8
46	20 Aug 1988	23:09:09.4	26.6N	86.7E	70	6.8
47	21 Mar 1988	23:31:20.3	77.6N	125.7E	9	6.2
48	20 Aug 1989	19:26:56.1	11.9N	41.8E	10	6.1
49	21 Aug 1989	01:09:05.7	11.8N	41.8E	10	6.3
50	12 May 1990	04:50:09.0	49.0N	141.8E	611	6.4
51	20 May 1990	02:21:59.7	5.0N	32.1E	7	6.6
52	14 Jul 1990	05:54:25.3	0.0	17.4W	10	6.4
53	06 Nov 1990	18:45:54.1	28.2N	55.4E	25	6.2
54	13 Jul 1991	02:50:14.5	42.1N	125.6W	10	6.4
55	14 Jul 1991	09:09:13.1	36.4N	71.1E	223	6.4
56	06 Aug 1991	02:17:32.5	3.8N	95.4E	25	6.0
57	17 Aug 1991	19:29:40.0	40.2N	124.3W	12	6.1
58	19 Okt 1991	21:23:15.5	30.7N	78.7E	19	6.5
59	19 Nov 1991	22:28:50.8	4.5N	77.4W	21	6.5
60	13 Dez 1991	02:33:52.3	45.5N	151.6E	32	6.2
61	13 Dez 1991	18:59:11.1	45.5N	151.7E	52	6.2
62	22 Dez 1991	08:43:13.3	45.4N	151.0E	26	6.3
63	02 Mar 1992	12:29:40.2	52.8N	160.0E	44	6.5
64	05 Mar 1992	14:39:10.2	52.9N	159.7E	44	6.5
65	25 Apr 1992	12:46:17.0	38.5N	14.9E	246	5.3
66	25 Apr 1992	18:06:04.2	40.3N	124.3W	15	6.4
67	26 Apr 1992	11:18:25.8	40.3N	124.5W	22	6.6
68	18 May 1992	23:19:20.0	7.5N	82.3W	11	6.0
69	20 May 1992	12:20:35.1	33.3N	71.2E	33	6.0
70	21 May 1992	04:59:57.5	41.5N	88.8E	0	6.6
71	28 May 1992	21:24:50.9	47.5N	155.6E	49	6.0
72	29 Jul 1992	04:30:49.3	39.4N	143.5E	29	5.9
73	30 Jul 1992	08:24:49.2	29.5N	90.1E	33	6.0
74	19 Aug 1992	00:57:43.6	50.4N	174.8W	33	6.1
75	19 Aug 1992	02:04:36.5	42.0N	73.5E	22	6.8
76	28 Aug 1992	18:18:45.3	0.9S	13.5W	10	6.4
77	11 Sep 1992	03:57:26.7	6.0S	26.6E	10	6.7
78	28 Sep 1992	14:06:02.8	24.1N	122.6E	29	5.9
79	17 Okt 1992	08:32:39.9	6.8N	76.8W	10	6.2
80	15 Jan 1993	11:06:05.0	42.9N	144.1E	100	6.9
81	07 Feb 1993	13:27:43.9	37.6N	137.2E	23	6.0
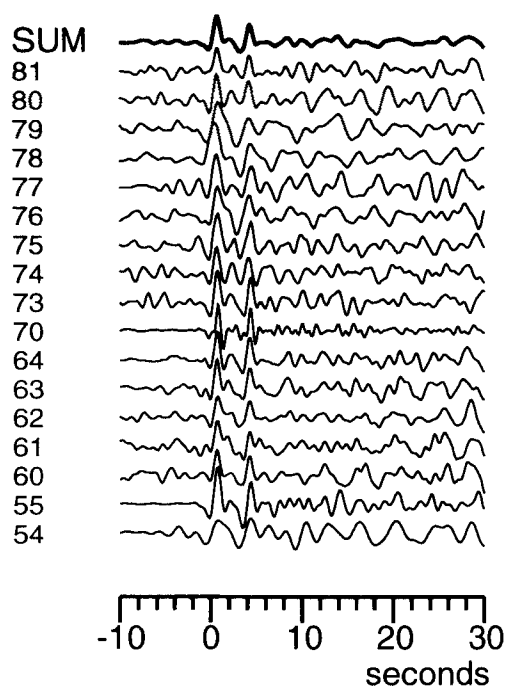
Figure 3. An example of the stacking of the deconvolved SV waveforms for station FUR. The event number at each trace refers to Table 1. The trace labelled SUM is the stacked SV waveform. The time $t = 0$ coincides with the maximum of the P wavelet on the L-component.

of the Q waveforms can be performed only for the Gräfenberg data. The GRSN stations do not yet have a sufficient data base for a dense azimuthal coverage. Fig. 6 shows the stacks of the averaged Gräfenberg traces in four quadrants of backazimuth. The difference in amplitudes is clearly seen for the east and west events. This difference can be explained by a laterally varying crustal structure under
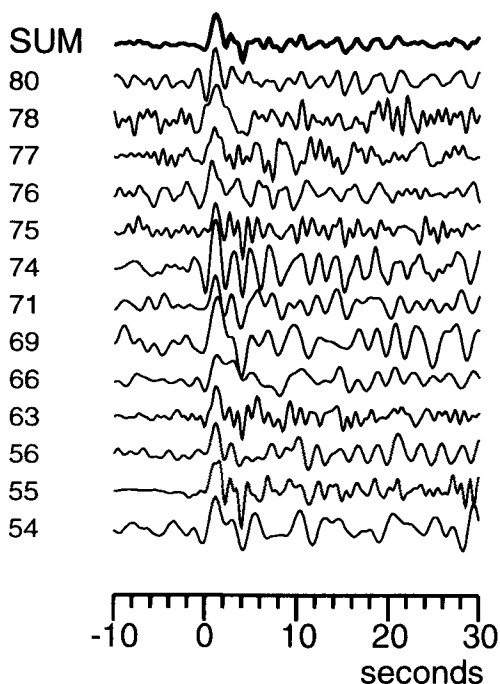
Figure 4. The same as in Fig. 3, but for station BRNL.

the Gräfenberg array. This point will be discussed again later.

FITTING OF GRSN DATA

Since the receiver function method is a steep-angle method, similar to the reflection method used in crustal studies, practically no absolute velocity information can be obtained (Ammon, Randall & Zandt 1990). Therefore the starting model for the inversion must be based on prior knowledge of a velocity model. The P-velocity–depth function from Mostaanpour (1984) was used to derive the starting model. This starting model was used for all stations; it resulted from a unified interpretation of many refraction lines in Germany. S-velocities were calculated using a v_P/v_S ratio of 1.8 in sediments and 1.73 in the rest of the crust. In the mantle, v_P/v_S was taken from IASP91 (Kennett 1991). The densities were calculated following Birch (1961). The velocity–depth functions were discretized by sampling the depth in layers of 0.5 to 2.0 km thickness.

The fitting of the observed Q waveforms was made in the time interval from -5 to 27 s. This interval includes all the crustal conversions and strongest multiples. The variable parameters are the S-wave velocities in 24 chosen homogeneous flat layers. The first 21 layers represent the crust to a depth of 35 km, and the three remaining layers the upper mantle. This set of variable parameters permits a search for the Moho discontinuity at any depth down to 41 km. The seismic stations have been divided into two groups according to different behaviour during inversion. For the first group, we had the best fits after a number of iterations from the starting model. The best solution had reasonable velocity values. Moderate changes of the starting model in this case do not dramatically change the final solution. These 'good' solutions were obtained for GRA1 (Fig. 7), GRS (sum of GRA1, GRB1 and GRC1, Figs 7 and 8), GRE (all events east of GRF, Fig. 8), BFO (Fig. 8), BUG (Fig. 9), CLZ (Fig. 9), TNS (Fig. 10) and WET (Fig. 10). For the remaining second group of stations, which includes FUR (Fig. 9), HAM (Fig. 10), GRB1 (Fig. 7), GRC1 (Fig. 7) and GRW (all events west of GRF, Fig. 8), we also obtained successful fits, but the S-velocities in some layers of the optimal model were unreasonable. Typical for this kind of instability are a number of alternating, thin, high- and low-velocity layers. In such cases we modified the starting model and started the inversion again. In the case of GRB1, the automated method did not improve the modified final model; therefore the lines for the starting and final models in Fig. 7 are nearly the same. The starting model was close to the final model of an earlier run, except that some alternating high- and low-velocity layers have been smoothed. We think that the fit is reasonably good.

For BRNL and HAM the reason for the initially unstable solution is very likely to be the presence of very thick low-velocity sediments. These sediments produce strong multiples over the entire record and mask the conversions and multiples from deeper discontinuities. For these two stations (Figs 10 and 9) we decreased the starting velocities in the upper six layers and obtained a successful and stable solution for the upper 15 km. For the lower crust at BRNL and HAM, the instability or the strong dependence of the solutions on the starting model makes the reliability of the
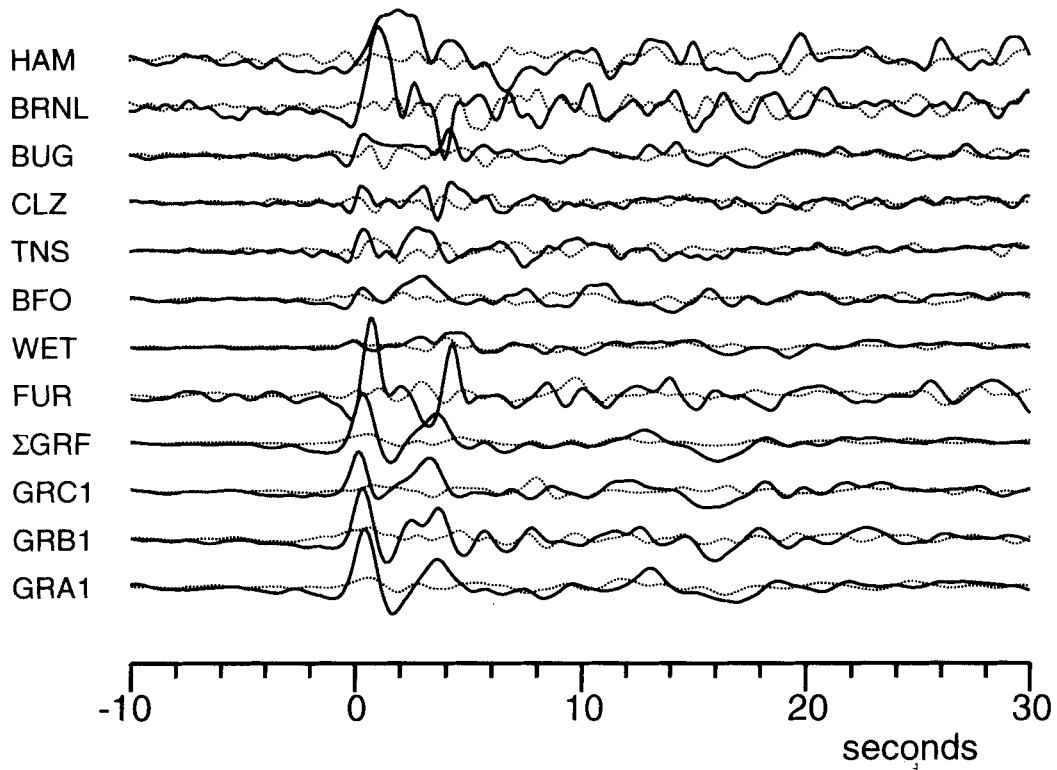
Figure 5. The results of stacking *SV*-waveforms (solid lines) and *T*-waveforms (dotted lines) for the GRSN stations. The trace labeled ΣGRF is the average of the Gräfenberg array.
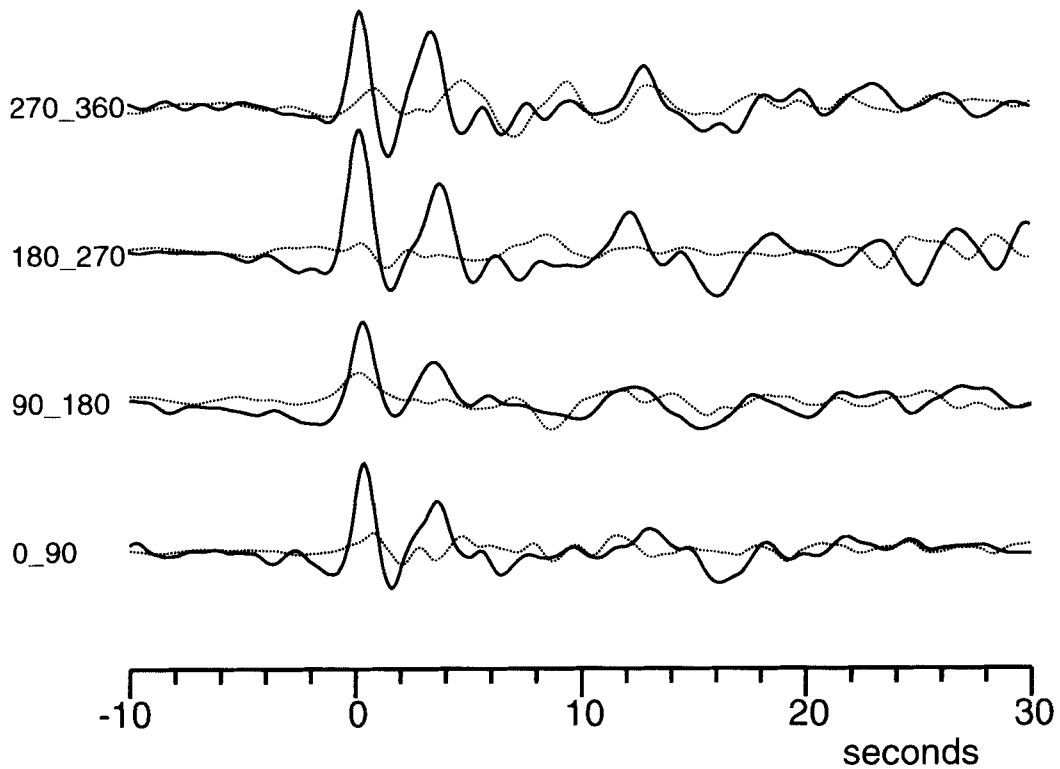

Figure 6. The results of stacking average Gräfenberg *SV*-components (solid lines) and *T*-components (dotted lines) in four different quadrants of back-azimuth (the numbers on the left of the traces give the azimuthal interval in °).
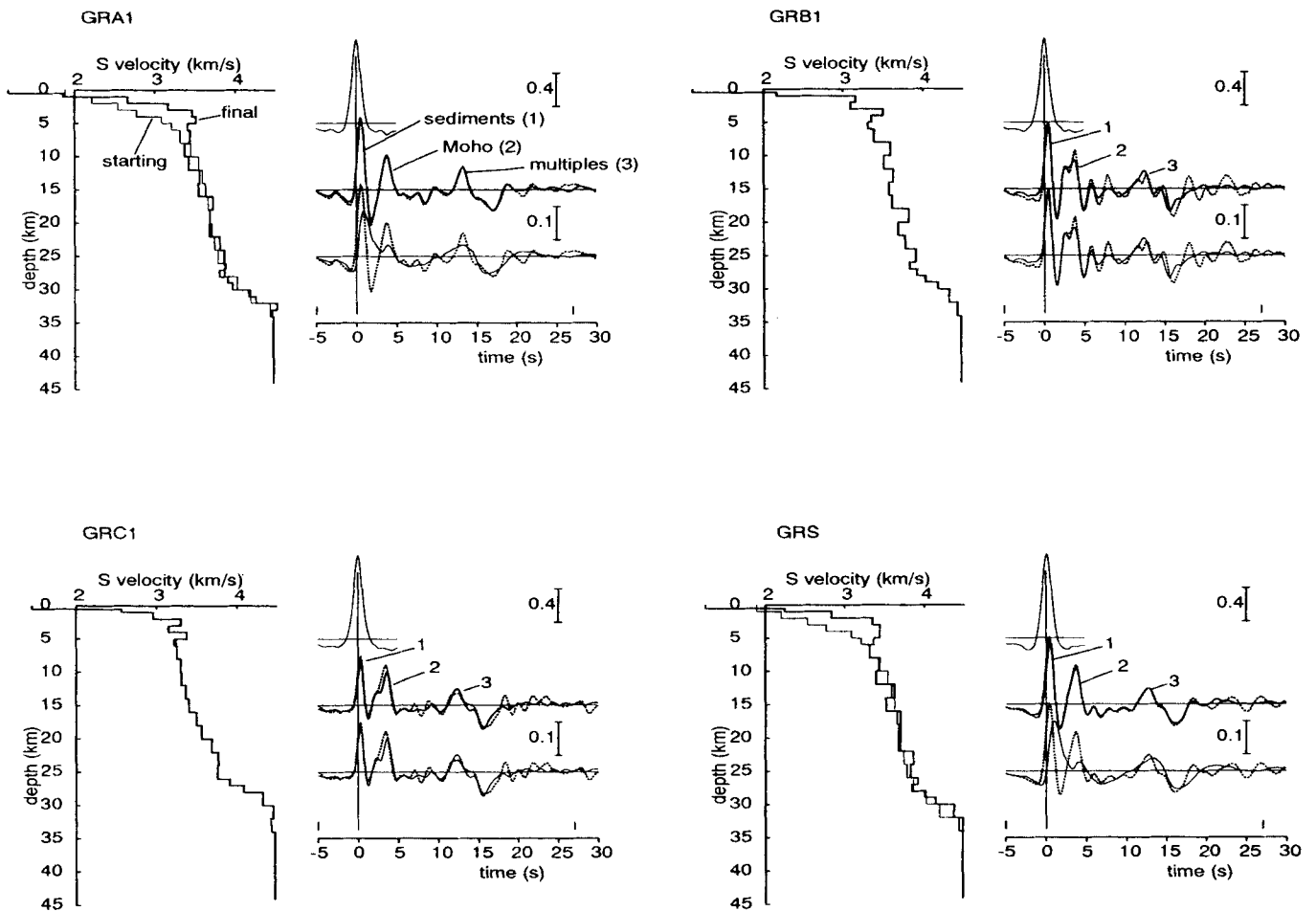
Figure 7. Results of the inversion for the Gräfenberg stations GRA1, GRB1 and GRC1 (upper left, upper right and lower left corners, respectively). The lower right corner shows, labelled GRS, the result that was obtained by using all three stations GRA1, GRB1 and GRC1 in the inversion. The starting velocity–depth model (thin line) and final model (thick line) are always shown to the left of the corresponding waveform plots. The uppermost spike-like waveform is the *P* wave form (*L*-component) obtained after deconvolution and stacking. The middle and bottom traces depict the observed and stacked waveforms on the *Q*-component (dotted lines) and, as solid lines, the synthetic waveforms for the starting model (bottom trace) and the final model (middle trace). Vertical bars placed just above the time axes indicate the inversion intervals. The normalized amplitudes are indicated by the vertical bars next to the waveform plots. The mean-square errors between observed and best-fitting waveforms are (in per cent of the maximum *P*-wave amplitude) 0.007, 0.018, 0.013 and 0.018, respectively. The labels applied to the middle traces in this and the following figures refer to the *P–SV* conversions from the base of the sediments (1), the Moho (2) and multiples between the free surface and Moho (3).

velocity–depth function questionable. For GRW, FUR, GRB1, GRC1 (Figs 8, 9, 7, 7 respectively) the first attempt of optimization gave a partly successful solution, where the velocities in a few layers were unreasonably high or low. In these cases we simply replaced the anomalous velocities by averaged values and started the inversion again, considering these modified models as new starting models. The inversion procedure was now successful in all these cases, and did not greatly change the parameters of the modified starting model.

DISCUSSION

First, the stations of the GRF array will be discussed.

GRA1 (Fig. 7). We obtained a Moho depth of about 32 km, similar to the depth obtained by Aichele (1976) from

a refraction profile directly west of GRF. Aichele's model will be discussed in more detail below. The Moho conversion is, as in nearly all data, a very clear phase. The most prominent phase in Fig. 7 is, however, the conversion at the bottom of the very low-velocity sediments. This feature at the sites of the GRF stations has been described by Krüger & Weber (1992) and Krüger (1994).

GRB1 and GRC1 (Fig. 7). We had problems inverting these data. The final model contained several alternating high- and low-velocity layers, which we thought were not real but rather a result of the inversion procedure. Therefore we arbitrarily smoothed the model and obtained nearly the same fit (the starting and final models in Fig. 7 are therefore nearly identical). For this reason we will only compare the Moho conversions at these stations. The Moho conversion at GRA1 has one clear pulse. There is a second pulse in front of the actual Moho conversion. The resulting
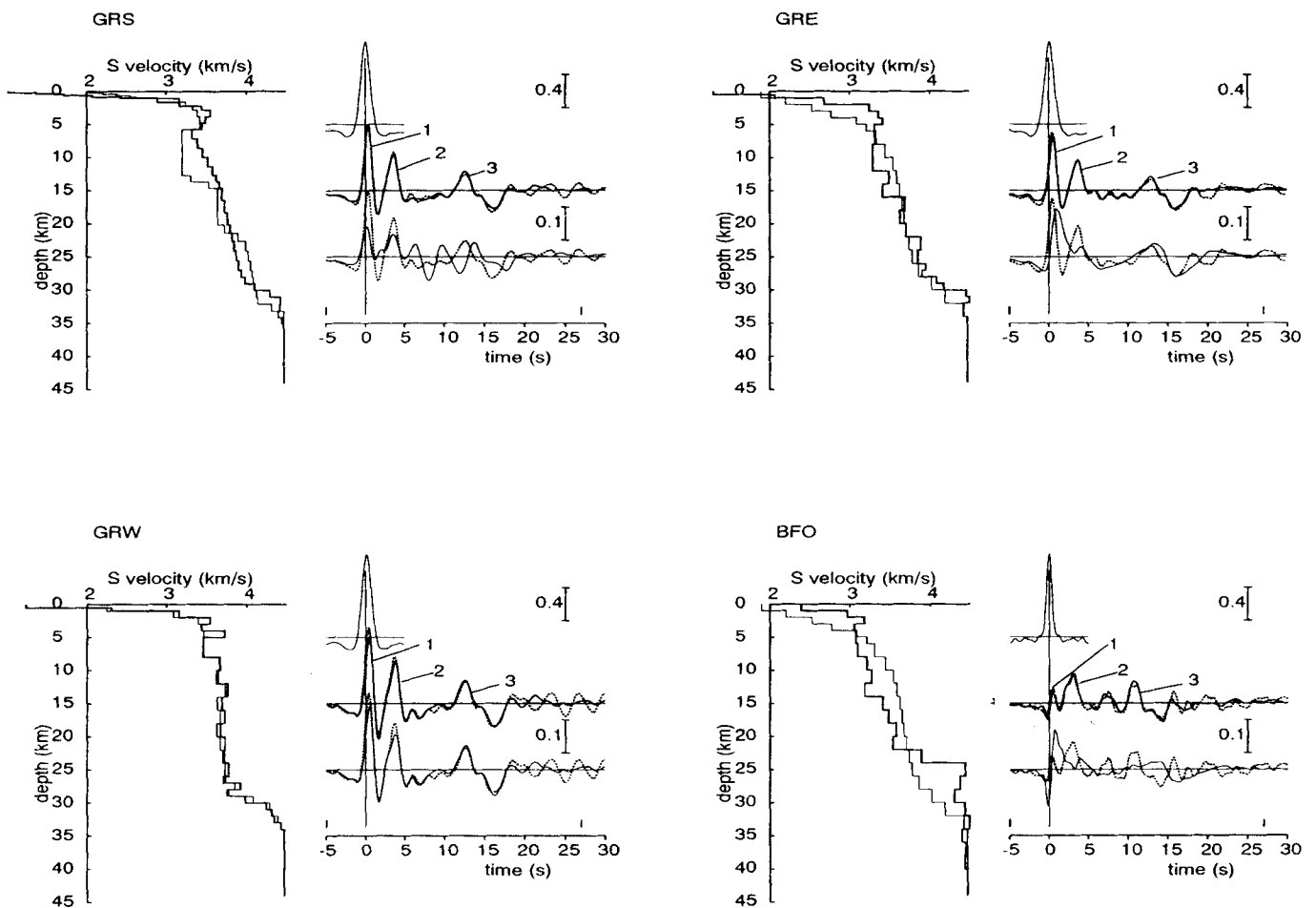
GRS

GRE

GRW

BFO

Figure 8. For the arrangement of panels and meaning of labels, see caption of Fig. 7.

GRS. Inversion of the GRS data using the Aichele (1976) refraction model as a starting model. The final model is very similar to the GRS model in Fig. 7. The main difference between the models by the refraction and receiver function methods is the large energy in the receiver function of the refraction model between about 4 and 10 s, which is not observed in the data. To obtain an acceptable fit, the sharp discontinuities of the Aichele model must be replaced by smoother transitions.

GRE. Inversion result using all three GRF stations and epicentres located to the east of GRF (labelled GRE). The mean-square error is 0.009.

GRW. Inversion result for the three GRF stations and epicentres to the west of GRF (labelled GRW). The mean-square error is 0.016.

BFO. Inversion result for station BFO. The mean-square error is 0.012.

models at these two stations have a less sharp Moho with higher velocity material 2–3 km above the Moho discontinuity.

GRS (Fig. 7). All GRF data have been summed to obtain an average model. This model contains two prominent features: the low-velocity sediments and a relatively clear Moho (the high-velocity Jurassic surface layer existing at the GRF stations is too thin to be seen by the 2–3 s period waves used in our study). The conversion from the basement–sediment discontinuity at the mean depth of 1 km arrives 0.3–0.4 s after the P onset. The Moho conversion arrives about 3.5 s after P. The main part of the crust consists of a fairly constant velocity gradient.

GRS (Fig. 8, compared with Aichele's refraction model). We have used Aichele's (1976) model obtained from a refraction profile as a second starting model for inverting the waveforms of the summed GRF records. The final model (GRS in Fig. 8) is very similar to the final model in Fig. 7, which was obtained from the standard starting model. This

means that our inversion procedure is fairly independent of the starting model. The Moho conversion in Aichele's model arrives at about the same time as in the final model; its amplitude is, however, too weak (also, the conversion at the bottom of the sediments is too weak in Aichele's model, but the sediments were certainly not a goal of the refraction profile). A significant difference between the refraction model and the receiver function model is that the refraction model produces internal multiples in the teleseismic data that are too strong. Also the Moho multiples do not arrive at the observed times. From these observations it can be concluded that the refraction model has contrasts in the interior of the crust that are too strong. The low-velocity layer is too pronounced. The teleseismic model is clearly smoother. The main periods of the teleseismic data are 2–3 s, whereas the refraction frequencies are several Hertz. Both methods certainly 'see' different things in the crust. Because of their longer periods, the teleseismic data are less sensitive to small-scale structure which can possibly be
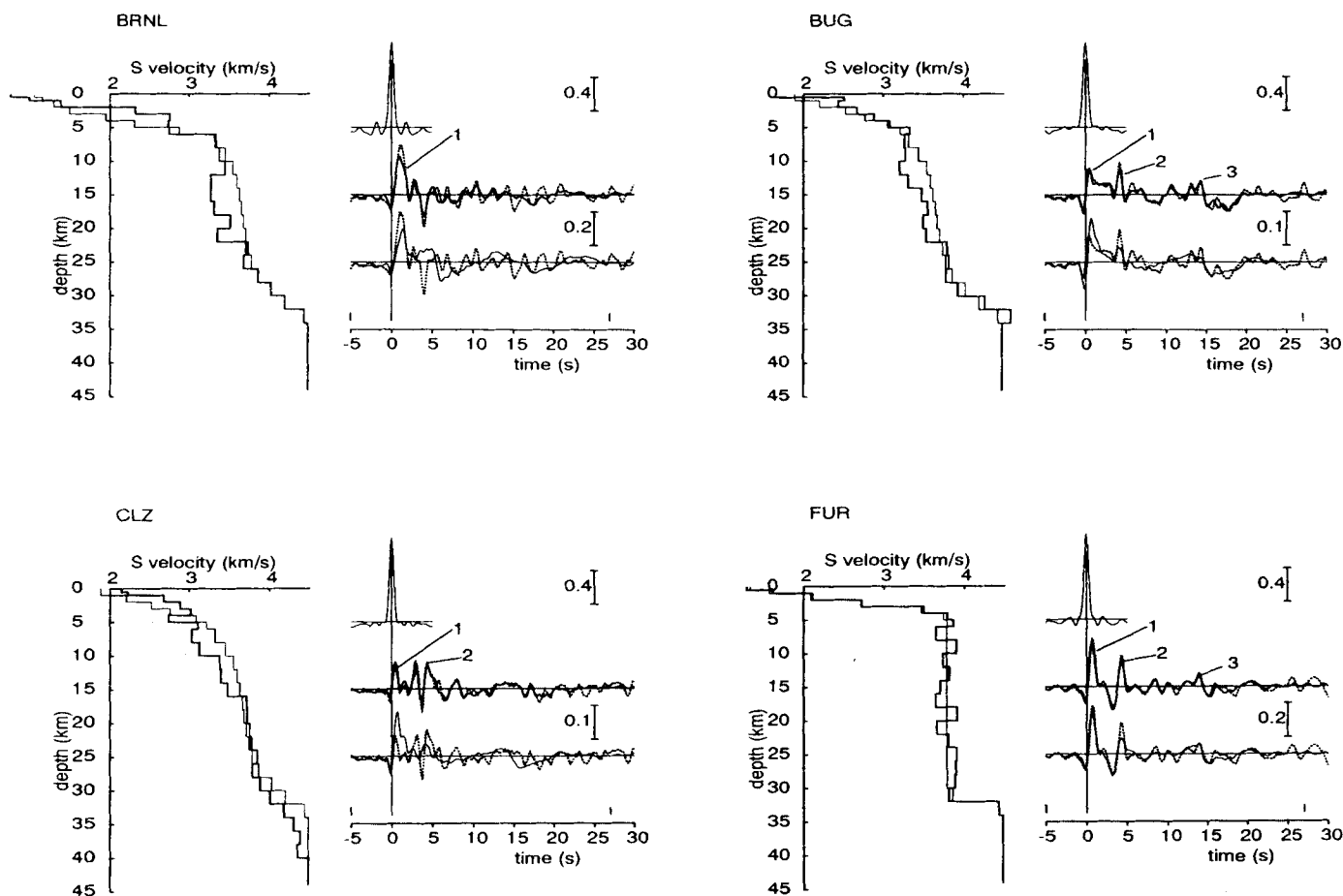
Figure 9. As Fig. 7, but for the stations BRNL, BUG, CLZ and FUR. Mean-square errors are 0.031, 0.010, 0.011 and 0.018, respectively.

resolved by refraction experiments. However, any existing model should also be able to explain the longer period teleseismic data. For this reason we can certainly conclude that the teleseismic model is a more realistic average model for the region of the GRF array.

GRE and GRW (Fig. 8). In GRE, all events with epicentres to the east of GRF have been summed for all three GRF stations, and GRW contains events in the west. Fig. 8 indicates that there is a stronger Moho conversion and stronger crustal multiples in GRW than in GRE. In Fig. 6, data from 90° sectors of back azimuth have been summed. This figure shows that the east–west difference is the main feature at GRF; more details seem difficult to resolve. For this reason we inverted the data for flat, layered models east and west of GRF. This can be considered as a first approximation of a general 3-D inversion. The resulting model for GRW has a more constant velocity through most parts of the crust and also more contrast at the Moho. No such distinction exists if events from the north or south are considered (see Fig. 6). For all other stations of the GRSN network, the data base is still too small for a study of the azimuth-dependent receiver function.

BFO (Fig. 8). The Moho is very sharp and at a relatively shallow depth (in agreement with Fig. 2). There is no sharp velocity contrast near the surface like there was at GRF. A constant gradient characterizes most parts of the crust.

BRNL (Fig. 9). Because the inversion was problematic, a

modified starting model was used. A reasonable agreement was only found after introducing thick sedimentary layers. The conversion at the bottom of the sediments and multiples in the sediments are the dominating features in the seismic record, as can be clearly seen in this figure. The sedimentary conversion arrives clearly later, and the signal width is larger than at other stations. The Moho is practically invisible, as the sediments produce high noise in the rest of the record and mask other signals.

BUG (Fig. 9). The Moho produces the strongest conversion, but the conversion at the bottom of the sediments is also strong. The Moho depth is about 32 km, a little larger than in Fig. 2.

CLZ (Fig. 9). There is a weak conversion at a discontinuity near the surface, and also a second conversion from the Moho. Crustal multiples are very weak (no energy later than 8 s). This results in a rather smooth crust–mantle boundary.

FUR (Fig. 9). Here we also had problems with the inversion. Although thick sediments, like at BRNL, produce strong reverberations, a sharp Moho signal is clearly visible. The Moho depth is 32 km, in agreement with Fig. 2. Crustal multiples are relatively weak, which could be explained by the gradual transition near the surface. A constant velocity is obtained for most parts of the crust beneath the sedimentary cover.

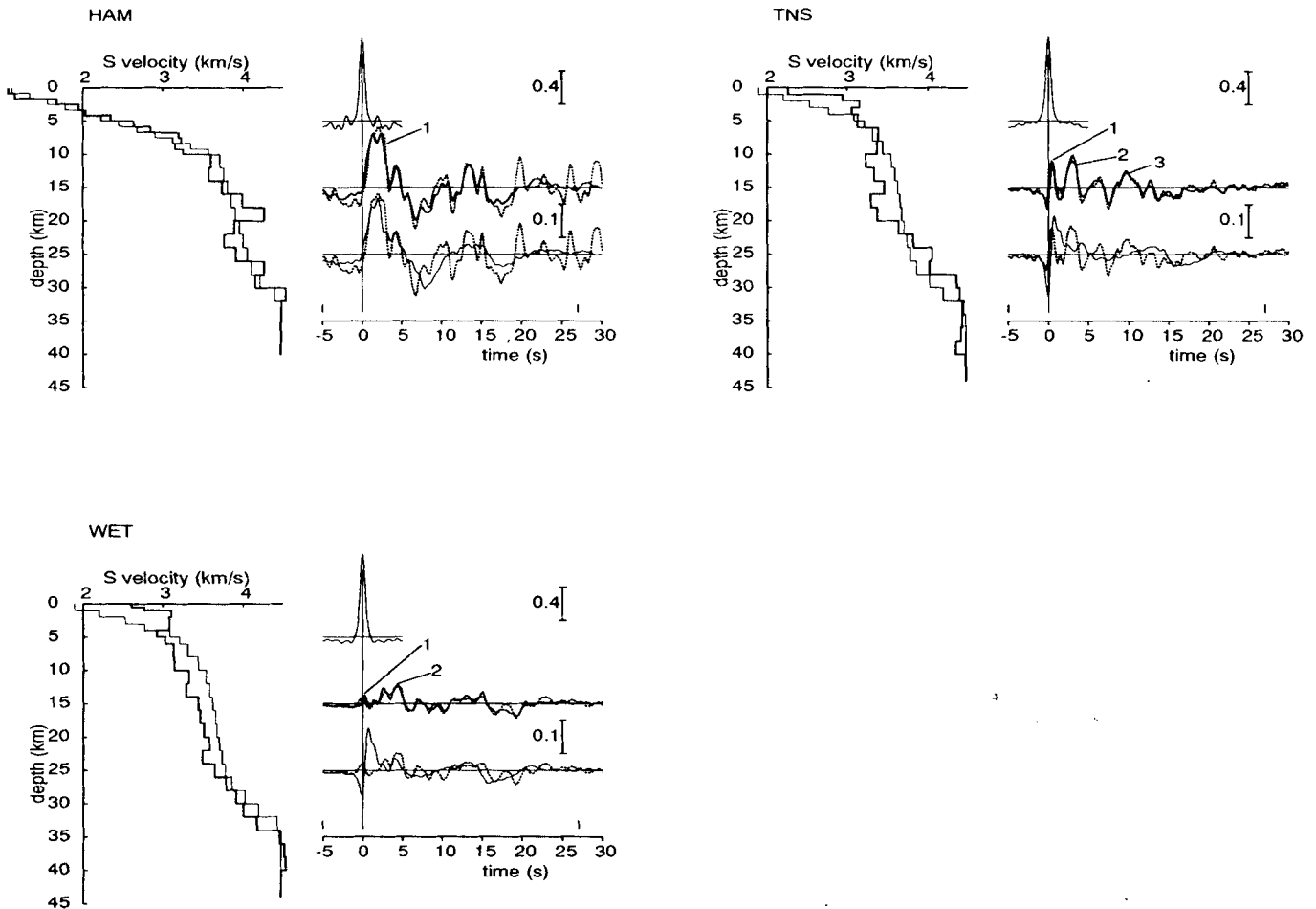HAM (Fig. 10). There were also problems with the

Figure 10. As Fig. 7, but for the stations HAM, TNS and WET. Mean-square errors are 0.026, 0.011 and 0.008, respectively.

inversion. Relative agreement could only be obtained after introducing low-velocity layers near the surface (thick sediments). These sediments mask everything else in the seismogram. The delay time of the sedimentary conversion at HAM is even larger than at BRNL. Also, the width of the sedimentary conversion signal is clearly the largest of all GRSN stations. We think, however, that a larger data base in the future could improve the results.

TNS (Fig. 10). Here we have a relatively strong and shallow Moho, in agreement with Fig. 2.

WET (Fig. 10). There is, as expected, no conversion from a near-surface sedimentary layer. The Moho conversion is, however, weak and very broad, indicating a smooth transition between that lower crust and mantle. This view is supported by the weak crustal multiples. The Moho depth is in good agreement with Fig. 2.

CONCLUSIONS

The receiver function method has proved to be very useful for the determination of crustal discontinuities. *P*-to-*S* conversions of teleseismic waves provide in nearly all cases information about the crust–mantle boundary and the sediment–basement boundary. Only at stations where thick sediments exist is the information from the lower crust masked by multiples in the sediments. There are also

indications that weaker discontinuities from within the crust may be detected if improved observational techniques, such as denser station spacing or observations of more events, are applied. New information can be provided by the receiver function method for the shear-velocity structure in the crust, which is only rarely obtained from other studies. The method can also serve to check crustal models obtained by other studies. It seems that, for the case of the refraction model obtained near Gräfenberg, the teleseismic model requires a smoother crust with less structure in its interior. A major new contribution of the receiver function technique is the easy observation of Moho conversions. Owing to the relatively steep angles of incidence of *P–S* conversion, the receiver function analysis provides a much higher horizontal resolution than refraction experiments. The improved resolution is of course not as good as in steep-angle controlled source experiments, but, since earthquakes are recorded, the signal-to-noise ratio is much less of a problem. A laterally very dense deployment of portable broad-band stations should provide new insight into many aspects of lithospheric structure. Another new contribution of the receiver function method is the observation of crustal multiples, which are very sensitive to sharp discontinuities and to strong gradients within the crust. These observations therefore narrow the range of possible crustal models. In all cases studied, the obtained crustal models are relatively

smooth, without sharp discontinuities. Pronounced low-velocity zones have not been found by our method, but this certainly does not rule out their existence. Examples of sharp and smooth crust–mantle boundaries are found in contrast to the smoother crustal interior.

ACKNOWLEDGMENTS

GLK and NVP were guest scientists at the GFZ Potsdam while this research was carried out. We thank P. Giese, Ch. Estabrook and G. Bock for reading the manuscript.

REFERENCES

Aichele, H., 1976. Interpretation refraktionsseismischer Messungen im Gebiet des Fränkisch-Schwäbischen Jura, *PhD thesis*, Universität Stuttgart.

Ammon, Ch.J., Randall, G.E. & Zandt, G., 1990. On the nonuniqueness of receiver function inversions, *J. geophys. Res.* **95,** 15 303–15 318.

Berkhout, A.J., 1977. Least square inverse filtering and wavelet deconvolution, *Geophysics,* **42,** 1369–1383.

Birch, F., 1961. The velocity of compressional waves in rocks to 10 kilobars, part 2, *J. geophys. Res.,* **66,** 2199–2224.

Blundell, B., Freeman, R. & Mueller, St., eds, 1992. *A continent revealed. The European Geotraverse,* Cambridge Univ. Press, Cambridge.

Burdick, L.J. & Langston, C.A., 1977. Modeling crustal structure through the use of converted phases in teleseismic body-waveforms, *Bull. seism. Soc. Am.* **67,** 677–691.

Cassidy, J.F., 1992. Numerical experiments in broadband receiver function analysis, *Bull. seism. Soc. Am.* **82,** 1453–1474.

Glasko, V.B., 1984. *Inverse problems of mathematical physics,* Moscow University, Moscow (in Russian).

Hanka, W., 1990. The German Regional Broadband Seismic Network (GRN) Project, *Workshop on MedNet,* pp. 83–95, eds Boschi, E., Giardini, D. & Morelli, A., Istituto Nazionale di Geofisica, Roma.

Haskell, N.A., 1962. Crustal reflections of plane P and SV waves, *J. geophys. Res.,* **67,** 4751–4767.

Kanasewich, E.R., 1981. *Time sequence analysis in geophysics,* The University of Alberta Press, Alberta.

Kennett, B.L.N. (ed.), 1991. *IASPEI 1991 Seismological Tables,*

Research School of Earth Sciences, Australian National University.

Kind, R. & Vinnik, L.P., 1988. The upper mantle discontinuities underneath the GRF array from P-to-S converted phases, *J. geophys.,* **62,** 138–147.

Kosarev, G.L., Makeyeva, L.I. & Vinnik, L.P., 1987. Inversion of teleseismic P-waves particle motions for crustal structure in Fennoscandia, *Phys. Earth planet. Inter.,* **47,** 11–24.

Kosarev, G.L., Petersen, N.V., Vinnik, L.P. & Roecker, S.W., 1993. Receiver function for the Tien Shan analog broadband network: contrast in the evolution of structure across the Talasso-Fargana fault, *J. geophys. Res.* **98,** 4437–4448.

Krüger, F. 1994. Sediment structure at GRF from polarisation analysis of P-waves of nuclear explosions, *Bull. seism. Soc. Am.,* **84,** 149–170.

Krüger, F. & Weber, M., 1992. The effect of low-velocity sediments on the mislocation vectors of the GRF array, *Geophys. J. Int.* **108,** 387–393.

Mostaanpour, M.M., 1984. *Einheitliche Auswertung krustenseismischer Daten in Westeuropa. Darstellung von Krustenparametern und Laufzeitanomalien,* Berliner Geowissenschaftliche Abhandlungen, Reihe B, Vol. 10, FU Berlin.

Owens, T.J., Zandt, G. & Taylor, S.R., 1984. Seismic evidence for an ancient rift beneath the Cumberland Plateau, Tennessee: A detailed analysis of broadband teleseismic P waveforms. *J. geophys. Res.* **89,** 7783–7795.

Petersen, N.V. & Vinnik, L.P., 1991. Detection of waves converted from P to SV in the crust by multichannel deconvolution, *Iz. Akad. Nauk SSSR, Fiz. Zemli,* **4,** 37–44 (in Russian).

Petersen, N.V., Vinnik, L.P., Kosarev, G., Kind, R., Oreshin, S. & Stammler, K., 1993. Sharpness of mantle discontinuities. *Geophys. Res. Lett.,* **20,** 859–862.

Phinney, R.A., 1964. Structure of the Earth's crust from spectral behavior of long-period body waves. *J. geophys. Res.* **69,** 2997–3017.

Stammler, K., Kind, R., Petersen, N., Kosarev, G., Vinnik, L. & Qiyuan, L. 1992. The upper mantle discontinuities: Correlated or anticorrelated? *Geophys. Res. Lett.* **19,** 1563–1566.

Tikhonov, A.N. & Arsenin, V.Y., 1979. *Methods of solutions of ill-posed problems,* Nauka, Moscow (in Russian).

Vinnik, L.P., 1977. Detection of waves converted from P to SV in the mantle, *Phys. Earth planet. Inter.,* **15,** 39–45.

Vinnik, L.P. & Kosarev, G.L., 1981. Determination of crustal parameters from observations of teleseismic body waves, *Proc. Acad. Sci. USSR,* **261,** 1091–1095 (in Russian).